## Supplementary Methods

### Supplementary Note 1

We performed a series of finite element (FE) simulations for the rolling depression of prelithiated anode to reveal both the kinematic details and underlying mechanisms of transfer-printing via the software COMSOL Multiphysics. During simulations, to ensure both efficiency and accuracy of calculations, we ignored the effect of inertial forces, considered the rollers as rigid bodies, and adopted the plane-strain hypothesis. As shown in Fig. 5a in the main text, we constructed the simulated system, which includes two rollers with a diameter of 5 cm, the lithium-coated copper foil (LiCF which consists of the lithium layer with a thickness of about 2 μm and the copper foil with a thickness of about 11 μm) and the graphite coated stainless steel (GrSS which consists of the graphite layer with a thickness of about 55 μm and the stainless steel layer with a thickness of about 20 μm). To describe the separation and adhesion behaviors of interfaces, we used a mixed-mode cohesive zone model involving both modes I and II interface fracture. The constitutive relationships of the interfaces are described by a bilinear traction-separation law. As shown in Supplementary Figure 27, the separation and traction of elements on the interfaces can be resolved into the normal component ($\delta_n, T_n$) and the tangential components ($\delta_t, T_t$) under the plane-strain condition, which are used to describe the mode I (opening) and II (shearing) interface fracture, respectively. The areas under the traction-separation curves in Supplementary Figure 27 represents the critical energy release rates ($G_n^C, G_t^C$). As illustrated in Supplementary Figure 27, the constitutive relationship is linearly elastic before the traction reaches the peak value ($T_n^0, T_t^0$). After the peak traction is attained, the traction linearly decreases with the increase of separation, indicating the interface failure. The quadratic failure criterion was used to characterize the damage initiation under the mixed-mode loading, and expressed as

$$\left(\frac{\langle T_n \rangle}{T_n^0}\right)^2 + \left(\frac{T_t}{T_t^0}\right)^2 = 1 \tag{1}$$

where $\langle\ \rangle$ denotes the Macaulay bracket, indicating that compression does not initiate damage. Once the traction reaches the peak value, the cohesive element starts to damage by reducing the stiffness by a factor of $1-d$, where $d$ is a damage variable and is defined as

$$d=\frac{\delta^f\left(\delta-\delta^0\right)}{\delta\left(\delta^f-\delta^0\right)} \tag{2}$$

where $\delta^0$ is the separation corresponding to the peak traction, $\delta^f$ is the complete separation (Supplementary Figure 27), and $\delta=\sqrt{\delta_n^2+\delta_t^2}$. The fracture criterion used in this work can be written as

$$\left(\frac{G_n}{G_n^C}\right)^2+\left(\frac{G_t}{G_t^C}\right)^2=1 \tag{3}$$

where $G_n$ and $G_t$ are the energy release rates in the normal and two tangential directions, respectively. When a certain amount of energy ($G_n^C$, $G_t^C$) is consumed, the traction is down to zero, meaning that the interface is completely broken.

During FE simulations, the transfer process is divided into two steps: firstly, reduce the gap between the rollers to compress the LiCF and the GrSS, and then rotate the roller to realize the transfer after reaching a certain compressive strain. A such two-step process is consistent with our experimental process. To ensure the accuracy of calculation, small enough incremental steps and thin enough mesh (the mesh size at the interface is about 1 μm) were used throughout simulations. In the compression stage, the compression increment is about 2 nm (equivalent to the compressive strain of about $2.5\times10^{-5}$). In the rotation stage, the rotation increment is about $5\times10^{-6}$ radian. During simulations, the stainless steel, the copper foil and the lithium are considered as isotropic and homogeneous linear elastic materials. Due to the characteristics of loose and porous graphite, the hyperelastic-ideal plastic constitutive model was used to describe the graphite. The hyperelastic part is described by a compressible neo-Hookean model and is determined by the following strain energy density function *W*,

$$W = \frac{1}{2}\mu\left(I_1 - 3\right) - \mu\ln\left(J\right) + \frac{1}{2}\lambda\left[\ln\left(J\right)\right]^2 \tag{4}$$

where $\lambda$ is the first Lamé constant, $\mu$ is the shear modulus or second Lamé constant, and $J$ is the Jacobian of the deformation gradient. Considering that the strength of lithium and copper foil obtained by electrodeposition are high considerably, it is assumed that the interface is not damaged during the simulation process. All the above simulation parameters were mainly obtained based on the experimental specimens or peeling experiments and listed in Table S2.

Supplementary Figure 32 shows a schematic illustration of simulation system for transfer-printing on the double-sided electrode. As shown in Supplementary Figure 32, the simulated system consists of two rollers with a diameter of 5 cm, the copper foil with thickness of 11 μm, two lithium layers with layer thickness of about 2 μm, two graphite layers with thickness of about 45 μm, and two stainless steel layers with layer thickness of 30 μm. Such system is fully consistent with the transfer-printing system shown in Fig. 6 in the main text. All the parameters (see Supplementary Table 2) used in the simulation of transfer-printing on the double-sided coated electrode sample are consistent with those used for the single-sided coated electrode sample. Supplementary Figure 33 shows a comparison in the shear stress distribution of the double-sided and single-sided coated electrode samples from simulation. It is seen in Supplementary Figure 33 that the shear stress distributions in these two simulated samples are very similar. Under the same conditions (including the same modulus and thickness of electrode, radius of roller, and shear strength between the stainless steel and graphite electrode), the critical compressive strain for the single-sided coated electrode sample is up to 0.221, which is close to that (0.225) for the double-sided coated electrode. It indicates that the single-sided or double-sided condition has no significant influence on the critical compressive strain for the separation between stainless steel and graphite electrode. Furthermore, due to the geometry symmetry of double-sided coated electrode, the shear stress distribution in the double-sided coated electrode exhibits an anti-symmetry with respect to both the horizontal and vertical symmetric axes. Notably, high shear stress is mainly concentrated at the interface between stainless steel and the graphite electrode, leading to a subsequent separation between stainless steel and the graphite electrode after transfer-printing. However, shear stresses at the graphite-lithium and lithium-copper interfaces are very

low. Thus, the graphite-lithium and lithium-copper interfaces always keep stable throughout transfer-printing.

To quantitatively characterize the separation between stainless steel and graphite electrode during transfer-printing, we established a theoretical model for the compression of two-layer film (including stainless steel and graphite electrode layers) under a roller, according to the experimental setup. Supplementary Figure 28 shows a schematic illustration of compression of two-layer film under a roller. The radius of roller is denoted by $R$, while the thickness of the stainless steel and graphite electrode is recemented by $H_0$-$h_0$ and $h_0$, respectively. According to our FE simulations, the separation between stainless steel and graphite electrode is mainly attributed to the shear stress generated at their interface during the compression under the roller. Therefore, we mainly considered the deformation of two-layer film under the compression of roller. The displacement fields at the interface between stainless steel and graphite electrode during deformation are continuous before the separation of interface. Note that the modulus of the stainless steel is much greater than that of graphite electrode. We assumed that the elastic deformation mainly occurs in graphite electrode and that the elastic strain energy is mainly stored in graphite electrode. These assumptions are reflected by the simulation results shown in Supplementary Figure 29. In Supplementary Figure 28, the X-Y and $x$-$y$ coordinates are used to describe the reference and present configurations, respectively. There exists a critical contact point between roller and compressed film. The position along $x$ axis of this contact point is denoted by $\mathrm{X}_c$. When the two-layer film is compressed by $\Delta h$ under the roller, the position of graphite electrode after deformation can be expressed by，

$$\begin{aligned} x &= \mathrm{X}\left[\frac{\mathrm{X}_c\left(R+h_0-\Delta h\right)-R^2\cdot\arcsin\left(\frac{\mathrm{X}_c}{R}\right)}{h}\right] \\ y &= \frac{\mathrm{Y}}{h_0}\left[h_0-\Delta h+2R\left(1-\cos\frac{\mathrm{X}}{R}\right)\right] \end{aligned} \tag{5}$$

Note that $x$ is much less than $R$, thus we adopted an approximation of $2R\left(1-\cos\frac{\mathrm{X}}{R}\right)\approx\frac{\mathrm{X}^2}{R}$. Then, the deformation gradient tensor can be written as,

$$\mathbf{F}=\frac{\partial \mathbf{x}}{\partial \mathbf{X}}=\begin{bmatrix}\frac{\partial x}{\partial \mathrm{X}} & \frac{\partial x}{\partial \mathrm{Y}}\\ \frac{\partial y}{\partial \mathrm{X}} & \frac{\partial y}{\partial \mathrm{Y}}\end{bmatrix}=\begin{bmatrix}\frac{\mathrm{X}_c\left(R+h_0-\Delta h\right)-R^2\cdot\arcsin\left(\frac{\mathrm{X}_c}{R}\right)}{h} & 0\\ \frac{\mathrm{Y}}{h_0}\frac{2\mathrm{X}}{R} & \frac{1}{h_0}\left(h_0-\Delta h+\frac{\mathrm{X}^2}{R}\right)\end{bmatrix} \tag{6}$$

The small deformation strain tensor is given by,

$$\boldsymbol{\varepsilon}=\frac{1}{2}\left(\mathbf{F}+\mathbf{F}^T\right)-\mathbf{I} \tag{7}$$

Combining Eq. (6) and Eq. (7), we obtained the following expressions of shear strain and stress,

$$\gamma_{xy}=\frac{\mathrm{Y}}{h_0}\frac{2\mathrm{X}}{R} \tag{8}$$

$$\tau_{xy}=\gamma_{xy}\mu=\frac{\mathrm{Y}}{h_0}\frac{2\mathrm{X}}{R}\mu \tag{9}$$

where $\mu$ is the shear modulus of graphite electrode. Eq. (8) describes the elastic shear stress distribution in graphite electrode. Supplementary Figure 30 shows a comparison of shear stress in graphite electrode from FE simulation and prediction from Eq. (8). It is seen from Supplementary Figure 30 that our theoretical prediction is close to FE simulation results, indicating the good validity and reliability of our theoretical model. Note that the maximum shear stress occurs at the critical contact point on the interface between stainless steel and graphite electrode, and can be expressed as,

$$\tau_{max}\big|_{\mathrm{X}=\mathrm{X}_c;\,\mathrm{Y}=h_0;}=\frac{2X_c}{R}\mu=\frac{2\sqrt{R\Delta h}}{R}\mu=\frac{2\sqrt{R\varepsilon_{com}H_0}}{R}\mu \tag{10}$$

where $\varepsilon_{com}$ represents the compressive strain of graphite electrode under the roller. In our simulations, we used the cohesive zone model to describe the interface between stainless steel and graphite layer. When the energy release rate in the interface exceeds a critical value, the stainless steel is separated from the graphite layer. Considering the complexity in the calculating the energy release rate in the interface, we introduced a simplified interface failure criterion: when the maximum shear stress on the interface exceeds the shear strength $T_t^0$ of interface (i.e. the peak

value of in the tangential traction in Eq. (1)), the graphite electrode separates from the stainless steel. Therefore, we obtained the following critical expression for the separation between stainless steel and graphite electrode,

$$\tau_{max} = T_t^0 \tag{11}$$

Plugging Eq. (10) into Eq. (11), we obtained the following critical compressive strain $\varepsilon_c$ for the separation between stainless steel and graphite electrode,

$$\varepsilon_c = \frac{R}{H_0}\left(\frac{T_t^0}{2\mu}\right)^2 \tag{12}$$

Note that both lithium and copper foils in the experimental system are much stiffer than the graphite layer, thus the deformation mainly occurs in the graphite layer. $H_0$ in the Eq. (12) can be replaced by the thickness $h_0$+$H$ of four-layer film (including stainless steel, graphite, lithium and copper foils) used in the experiments, where $H$ is the thickness of film including stainless steel, lithium and copper foils. Thus, the critical compressive strain is given by,

$$\varepsilon_c = \frac{R}{h_0 + H}\left(\frac{T_t^0}{2\mu}\right)^2 \tag{13}$$

Eq. (13) indicates that the critical compression strain for the separation between stainless steel and graphite electrode is determined by the thickness and shear modulus of electrode, the radius of roller, and the shear strength of interface between stainless steel and electrode. Fig. 5g-i in the main text and Supplementary Figure 31 show the comparisons between theoretical predictions and FE simulations, indicating that the predictions from our theoretical model are in good agreement with the FE simulation results.

The electrode production rate of the system is measured as 360 cm $h^{-1}$. The electrode production rate in RET system is mainly restricted by the transition speed of copper substrate in a continuous electrodeposition process. The speed of the electrodeposition process can be obtained from the following equation,

$$v = \frac{lj}{q} \tag{14}$$

where $v$ (in unit of cm/h) refers to the transition speed of copper substrate in continuous electrodeposition process, $l$ (in unit of cm) refers to the length of the copper substrate immersed in electrolyte, $j$ (in unit of mA $cm^{-2}$) refers to the current density of electrodeposition, and $q$ (in unit of mAh $cm^{-2}$) refers to the quantity of electric charge of electrodeposited lithium. The value of $q$ is determined by the type and area loading of the anode active materials. The loading of active material (graphite) is about 3.3 mg $cm^{-2}$. $q$ can be controlled by the current of the power supply. The value of $j$ can be adjusted in a certain range from 1 mA $cm^{-2}$ to 20 mAh $cm^{-2}$. The value of $l$ is measured as 25cm in RET system. The value of $v$ can be adjusted from 200 cm $h^{-1}$ to 6000 cm $h^{-1}$.

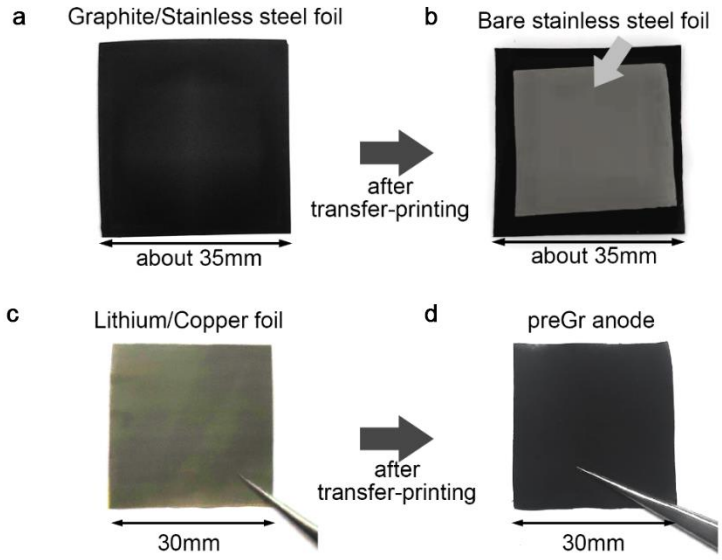


**Supplementary Figure 1 | a,** Photograph of Graphite on stainless steel foil (GrSS). **b,** Photograph of GrSS after transfer-printing. A quadrate area of the graphite layer is tidily removed from the surface of the stainless steel. **c**, Photograph of lithium-deposited copper foil (LiCF). **d**, Photograph of preGr electrode.

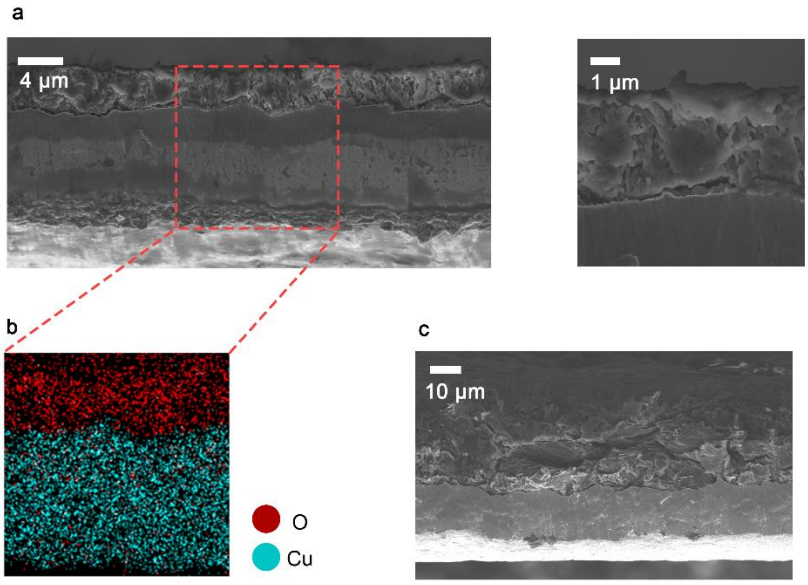


**Supplementary Figure 2 | a**, Cross-sectional SEM image of lithium deposited on copper foil. The lithium layer was electrodeposited on the upper surface of the copper foil. The capacity of deposited lithium is about 0.4 mAh $cm^{-2}$. The amplification SEM image shows the clear dividing line of the copper and lithium layer. The deposited lithium presented a loose columnar growth pattern. **b**, EDS image of lithium deposited on copper foil. There is a clear demarcation of the O and Cu signals representing the boundary of lithium and copper foil. The lithium layer exhibits a strong oxygen signal of O because of the SEI formed during electrodeposition on the surface of lithium. **c**, Cross-sectional SEM image of GrSS. The original thickness of the graphite layer is about 60 μm.

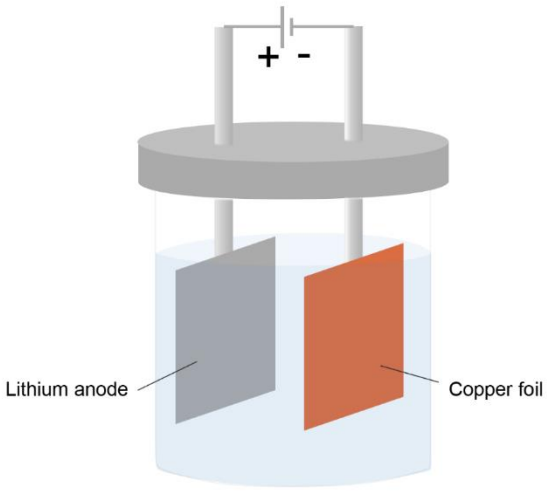


**Supplementary Figure 3** | Schematic diagram of lithium deposition step. Electrodeposition is accomplished through a direct current power supply. A lithium foil (1mm thick) was used as the anode and a copper foil with one side protected by polyimide tapes were used as the cathode. The polyimide tapes were removed before the cleaning step. The area of the copper foil immersed in the electrolyte is $3 \times 3$ $cm^2$.

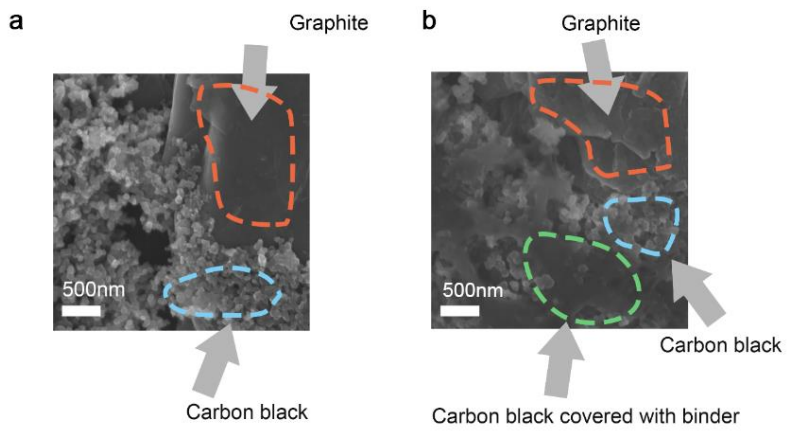


**Supplementary Figure 4** | **a**, Surface details of Gr anode. **b**, Surface details of 30 preGr anode. The orange marks in both images show the large graphite block. The blue marks show the conductive carbon black on the surface. The green mark shows the PVDF binder covered on the surface. For common Gr anodes, relatively significant graphite gains and fractal-like conductive carbon black make up the surface. Nevertheless, in the 30 preGr anode, some parts of the carbon black are covered with PVDF binder because of the nonuniform distribution of binder during the drying process.

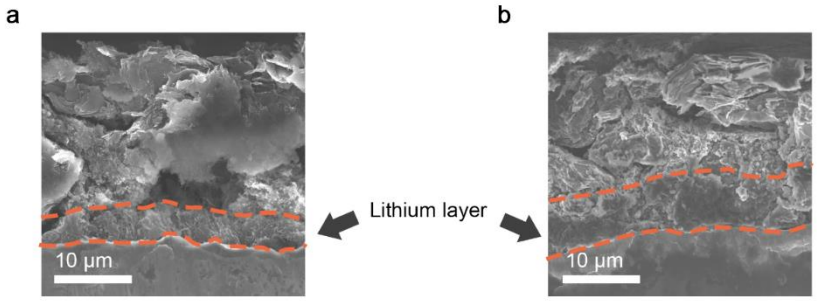


**Supplementary Figure 5 | a**, Cross-sectional SEM image of the 50 preGr electrode. **b**, Cross-sectional SEM image of the 100 preGr electrode. With the increasing lithium capacity, the thicknesses of the lithium layer increase.

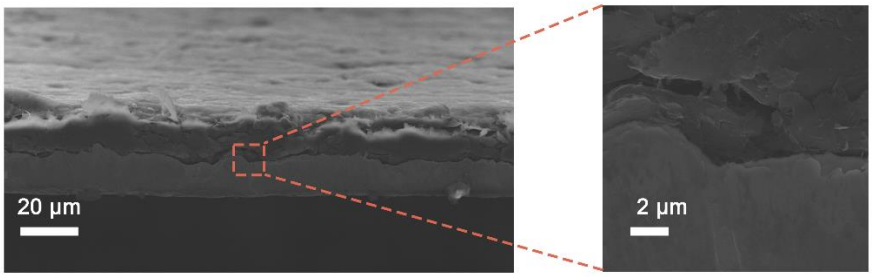


**Supplementary Figure 6** | Sectional-view SEM images of 30 preGr electrodes after prelithiation reaction. There is no visible lithium layer in the 30 preGr electrodes after the prelithiation reaction. The adhesion between the copper substrate and graphite layer would be weakened because of the disappearance of the lithium layer. However, no drawbacks were detected in the specific capacity, rate capability or cyclic stability of pGr electrodes. The pressure applied in the coin cell preserved good contact between the copper substrate and graphite layer. The pressure in cells would help the electrode maintains good performance.

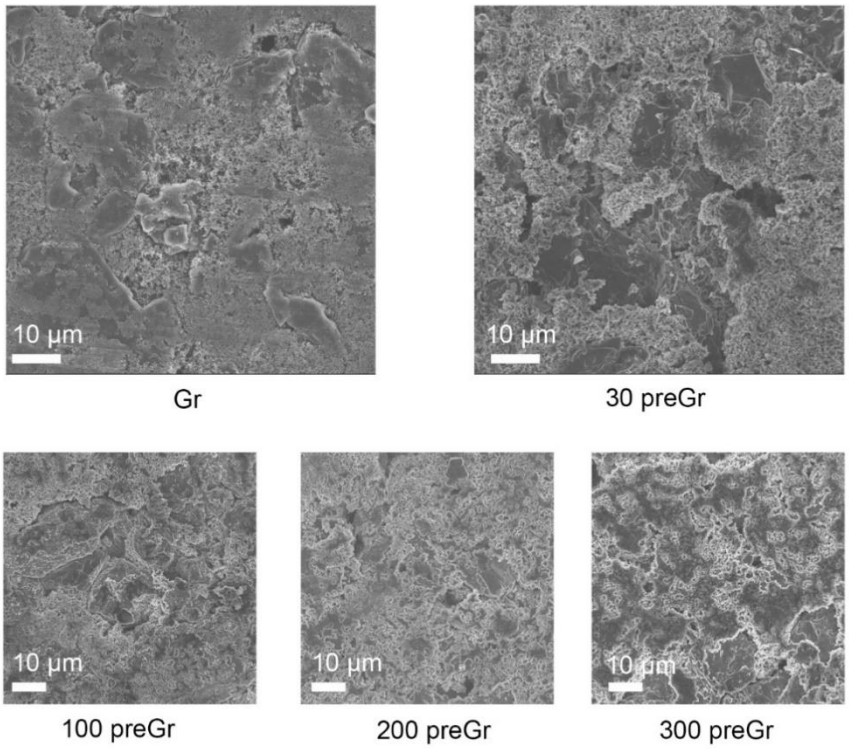


**Supplementary Figure 7** | Surface SEM images of Gr, 30 preGr, 100 preGr, 200 preGr, and 300 prGr anodes after the prelithiation reaction. Although the Li-GICs formed in these electrodes, the structure of these electrodes did not change.

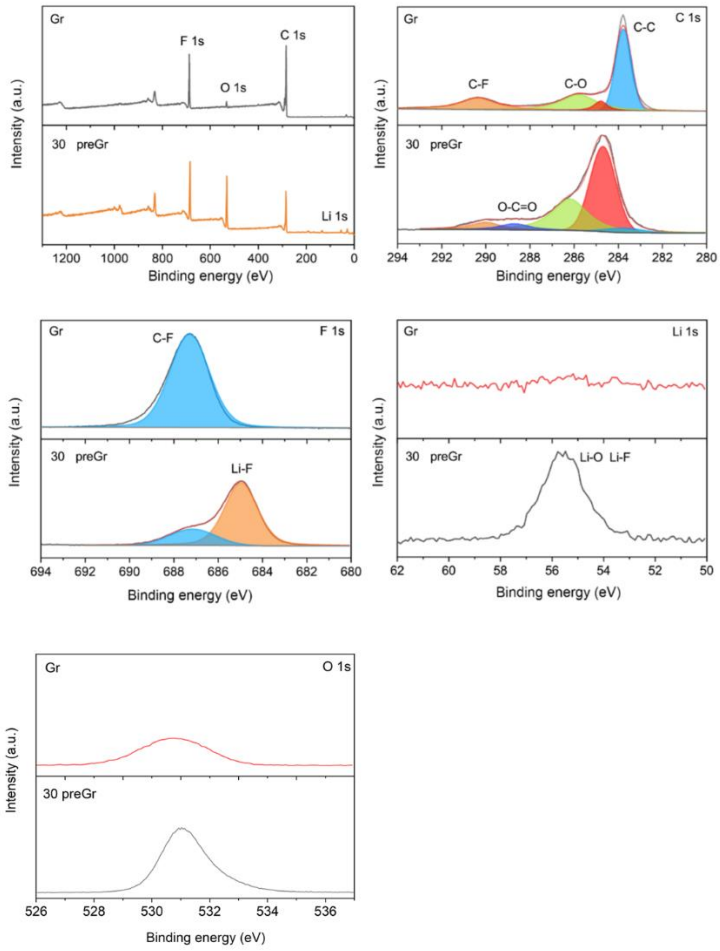


**Supplementary Figure 8 |** XPS spectra of Gr and 30 preGr anodes after prelithiation reaction. The full spectrum shows that the intensity of C was weakened, and the intensity of O was largely enhanced after the prelithiation reaction. These indicated that large amounts of oxygen-contained compounds formed during the reaction. The blue and red peaks in C1s branches may correlate with different types of C-C bonds.

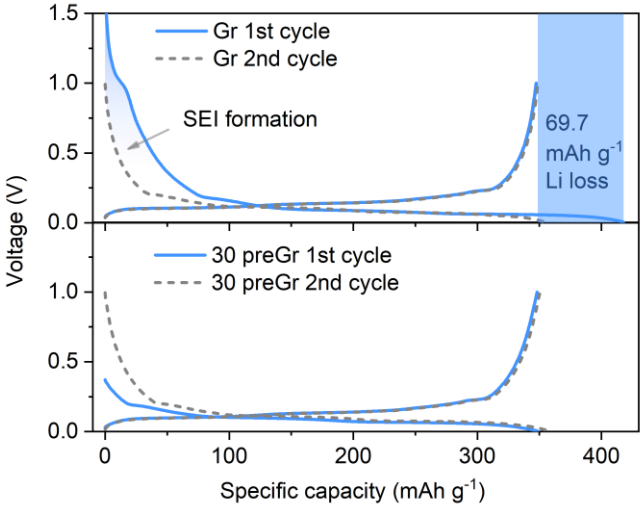


**Supplementary Figure 9** | Voltage profiles for the first two cycles of Gr and 30 preGr electrode half cells. The prelithiation reaction compensate for a lithium loss of 69.7 mAh $g^{-1}$. The profiles of the second cycle of Gr and 30 preGr cells are similar. In the first cycle of the Gr profile, the platform at 1.0 V is correlated with the SEI formation.

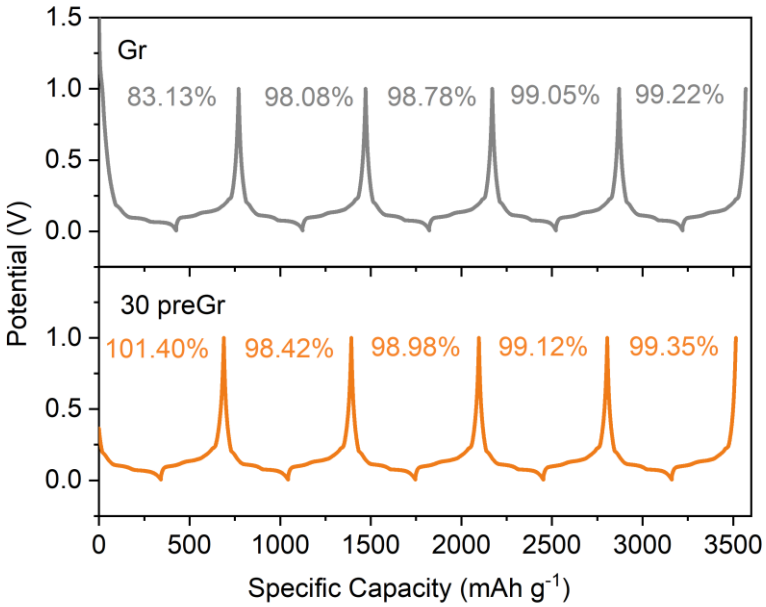


**Supplementary Figure 10** | Comparison of coulombic efficiencies of Gr and 30 preGr electrodes during the first few cycles. For the first cycles, the coulombic efficiencies of 30 preGr cells are higher than the Gr one, indicating that the lithium compensation of the prelithiation reaction can also offset parts of the lithium loss in the following cycles.

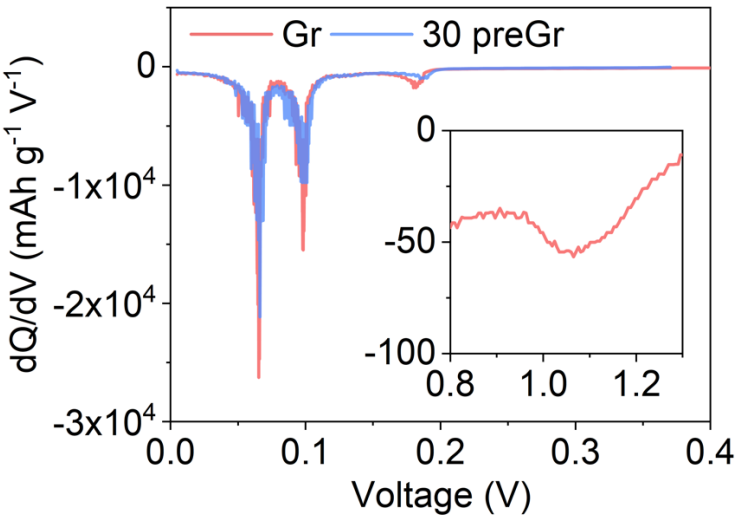


**Supplementary Figure 11** | Differential capacity (dQ/dV) plots of Gr and 30 preGr electrodes at the first lithiation process.

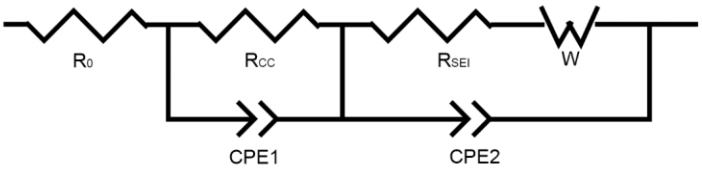


| Sample | Condition | $R_0$(Ω) | $R_{CC}$(Ω) | $R_{SEI}$(Ω) |
|---|---|---|---|---|
| Gr | 1st cycle | 4.22 | 3.61 | 20.46 |
| | 10th cycle | 4.91 | 4.11 | 15.80 |
| | 100th cycle | 7.27 | 8.47 | 9.89 |
| 30 preGr | 1st cycle | 4.96 | 3.52 | 15.35 |
| | 10th cycle | 5.39 | 6.38 | 9.89 |
| | 100th cycle | 6.01 | 7.41 | 9.30 |

**Supplementary Figure 12 |** Equivalent circuits of Gr and 30 preGr anodes. The $R_0$ and $R_{CC}$ of both Gr and 30 preGr electrodes were similar and rose gradually during the circulation. However, the $R_{SEI}$ of the 30 preGr electrode was significantly lower than the Gr one at the 1$^{st}$ and 10$^{th}$ cycles. The $R_{SEI}$ of both electrodes tended to be the same after 100 cycles. The gradual decrease of RSEI of both electrodes shows that the SEI with high conductivity was generated during the circulation.

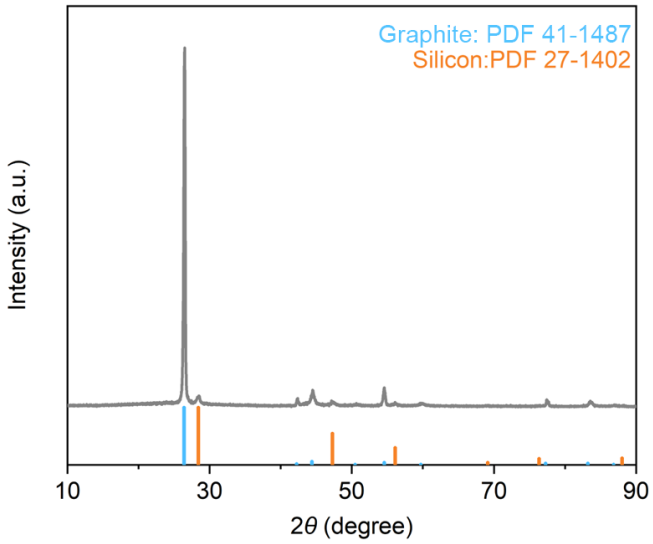


**Supplementary Figure 13** | XRD pattern of Si/C material. The Si percentage was 7.43 wt% by inductive coupled plasma emission spectrometer.

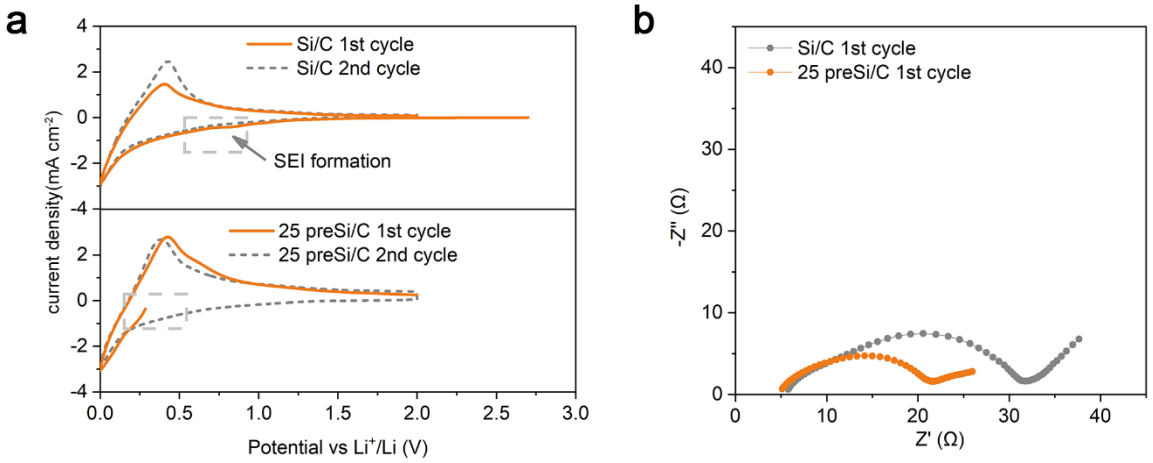


**Supplementary Figure 14 | a**, CV curves of Si/C and 25 preSi/C electrodes. **b**, Equivalent circuits of the Si/C and 25 preSi/C half cells after one cycle. The two anodes share a similar CV pattern, i.e., a reduction slope from 0.5 to 0 V and a single oxidation peak at about 0.45 V. However, the Si/C anodes own another reduction peak at about 1.0 V due to the SEI formation at the surface of electrodes. Furthermore, a larger increase at the oxidation peak in subsequent scans reveals worse reversibility than the 25 preSiC anode. The 25 preSi/C anode has a lower $R_{SEI}$ after the first cycling.

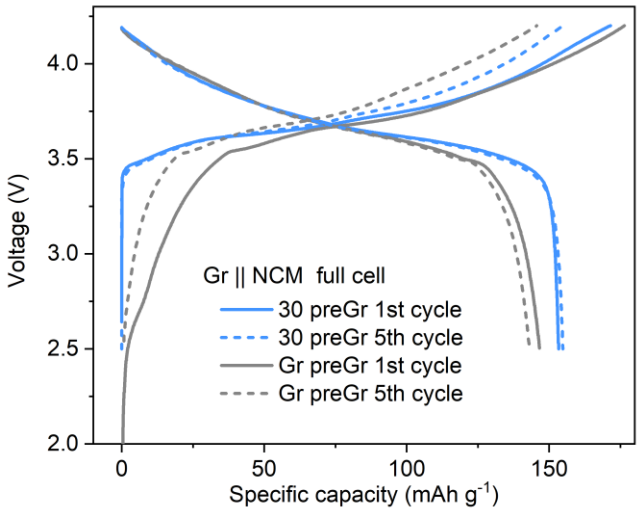


**Supplementary Figure 15** | Voltage profiles for the 1st and 5th cycle of Gr||NCM and 30 preGr||NCM full cells. The Gr||NCM cell shows a more series capacity loss than the 30 preGr||NCM cell during the first five cycles due to the continuous lithium loss in these cycles.

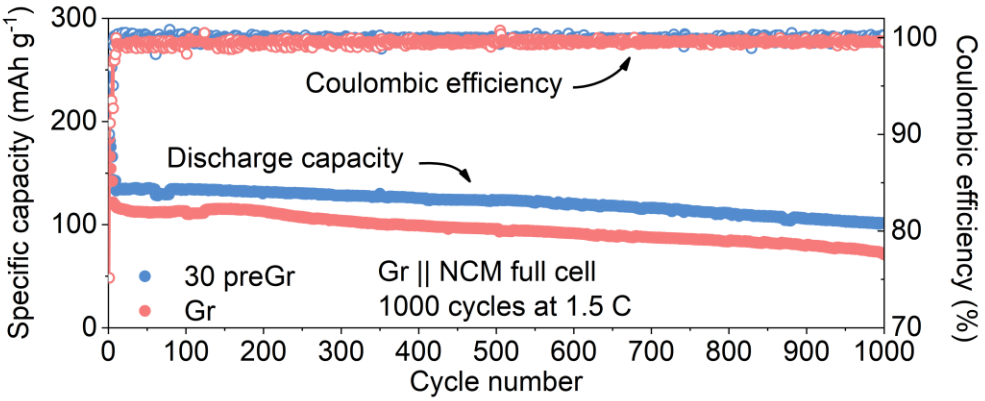


**Supplementary Figure 16** | Galvanostatic cycling of the Gr || NCM and 30 preGr || NCM full cells at 1.5C For these cells, 1C = 200 mAh $g^{-1}$ based on cathodes. These cells were first activated at 0.05C for one cycle, 0.1C for one cycle, 0.2C for one cycle, 0.4C for two cycles, 0.8C for four cycles and worked at 1.5C.

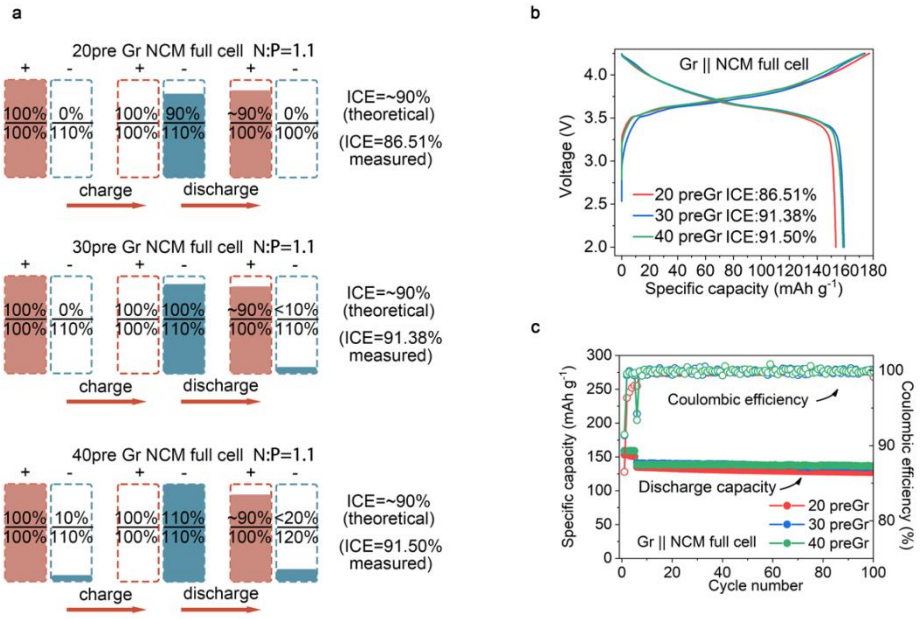


**Supplementary Figure 17** | **a**, The schematic diagram of lithium-ion migration in the NCM full cells with 20 preGr, 30 preGr, and 40 preGr anodes at the first cycle. **b**, Voltage profiles of the NCM full cells with 20 preGr, 30 preGr, and 40 preGr anodes. **c**, Galvanostatic cycling of the NCM full cells with 20 preGr, 30 preGr, and 40 preGr anodes. The cells were activated at 0.1C for five cycles and then worked at 0.5C. For these cells, 1C = 200 mAh $g^{-1}$ based on the cathode. In theory, these cells would show similar ICEs and discharge capacities. However, the 20 preGr full cells delivered a lower discharge capacity and ICEs than expected. Further cycle stability test shows that the discharge capacity of the 20 preGr full cell at 0.5C is slightly lower than the 30 preGr and 40 preGr full cells. These could be ascribed to the lithium loss of SEI formation in the first five cycles. It could be observed that the coulombic efficiencies of 20 preGr cells were much lower, and the discharge capacities decreased faster than 30 preGr and 40 preGr full cells in the first five cycles. In 30 preGr and 40 preGr full cells, the redundant lithium-ions could help compensate for the continuous lithium loss in the first five cycles. For 40 preGr cells, there are risks of lithium plating theoretically and cost disadvantages of introducing more lithium. In conclusion, the 30 preGr||NCM full cells are the best choices for demonstrating the performance of our prelithiated full cells.

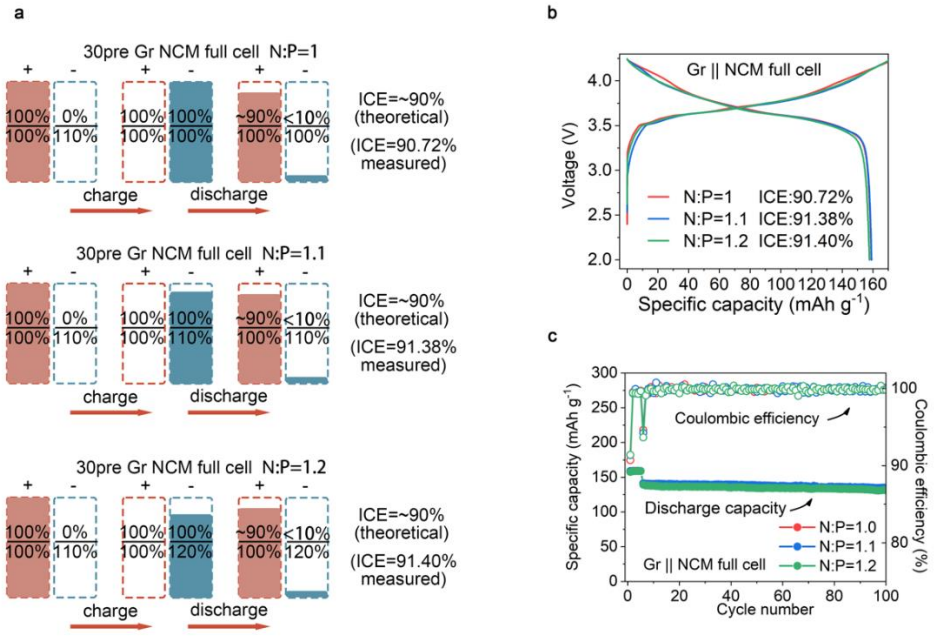


**Supplementary Figure 18** | **a**, The schematic diagram of lithium-ion migration in the NCM full cells with NP ratios of 1.0, 1.1, and 1.2 at the first cycle. **b**, Voltage profiles of the 30 pre Gr || NCM full cells with NP ratios of 1.0, 1.1, 1.2. **c**, Galvanostatic cycling of the 30 preGr || NCM full cells with NP ratios of 1.0, 1.1, 1.2. The cells were activated at 0.1C for five cycles and then worked at 0.5C. For these cells, 1C = 200 mAh $g^{-1}$ based on the cathode. In theory, similar ICEs and discharge capacities were expected for these cells. Significantly, there is an obvious risk of lithium plating on anodes for full cells with NP ratios of 1.0 in the first charge process and following cycles leading to a potential safety hazard. A slight peak was observed in figure b at the voltage of about 4.0V for the N:P=1.0 profile compared to other profiles. The small peak indicates the lithium plating reaction in full cells with NP ratios of 1.0. Comparing the first cycles with NP ratios of 1.0, 1.1, and 1.2, similar ICEs and discharge capacities were demonstrated as expected. Figure c also shows similar cycle stabilities in these cells. Therefore, the full cell with NP ratios of 1.1 has apparent advantages in view of safety and energy density compared to those with NP ratios of 1.0 and 1.2.

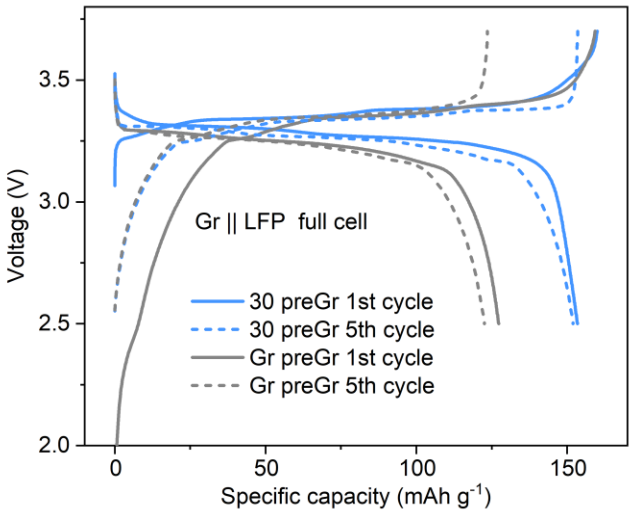


**Supplementary Figure 19** | Voltage profiles for the 1st and 5th cycle of Gr||LFP and 30 preGr||LFP full cells. The Gr||LFP cell shows a more series capacity loss than the 30 preGr||LFP cell during the first five cycles due to the continuous lithium loss in these cycles.

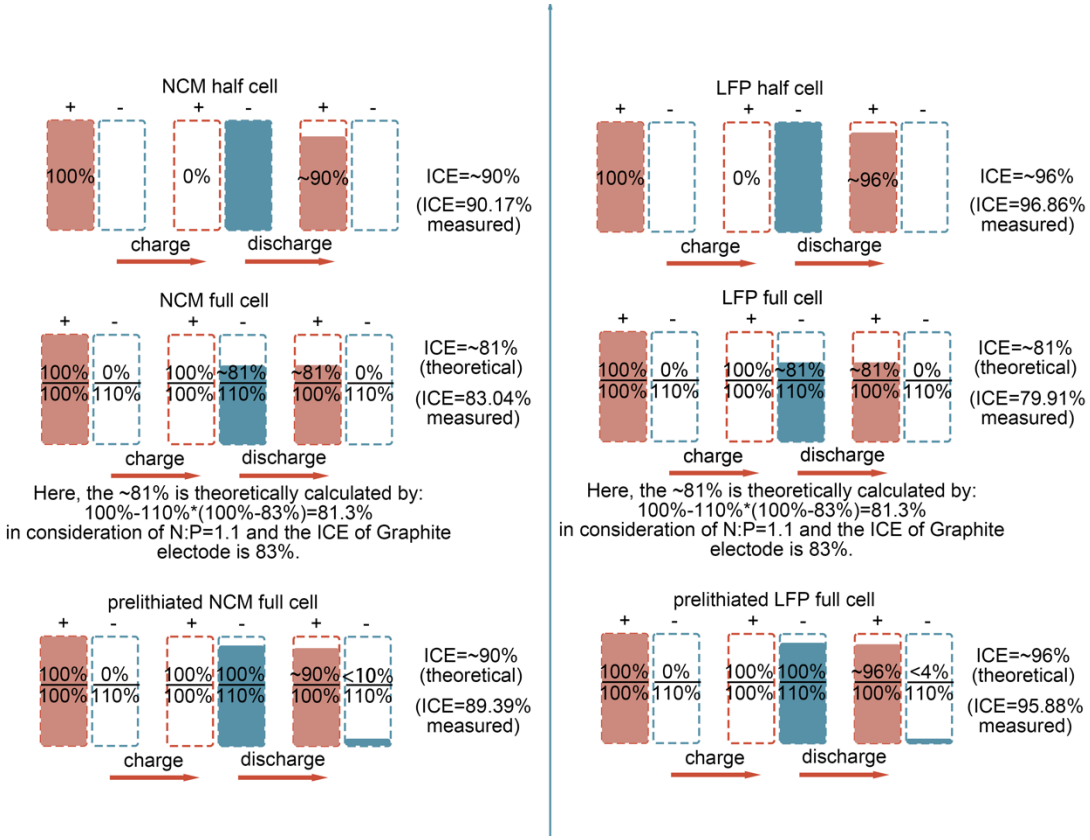


**Supplementary Figure 20** | The schematic diagram of lithium-ion migration in the NCM and LFP full cells. In the first cycle, the lower ICE of the NCM half cell means a higher amount of reversible lithium-ions cannot insert again into the NCM cathode at the end compared to LFP cells of the first charge-discharge cycle. The low ICE of the NCM half cell originates from the slow migration of a part of the lithium-ions in the NCM cathode. This part of reversible lithium-ions, which cannot insert in NCM, compensates the lithium loss in graphite electrodes in another way.

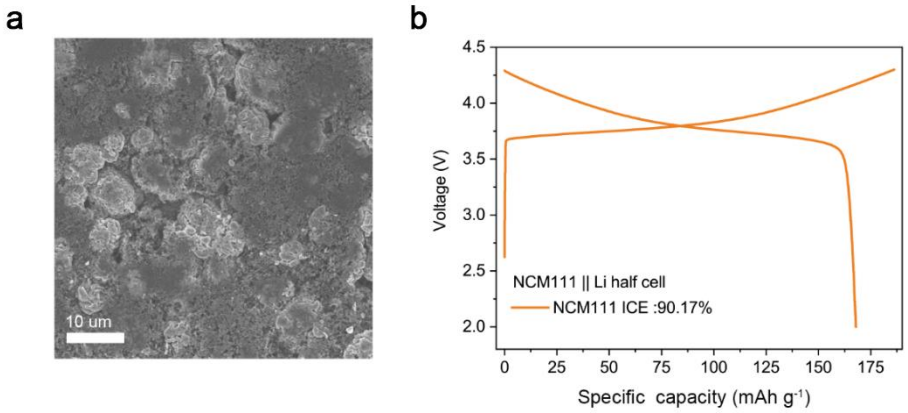


**Supplementary Figure 21** | **a**, Typical SEM image of the NCM electrode. **b**, Voltage profiles of the NCM half cell.

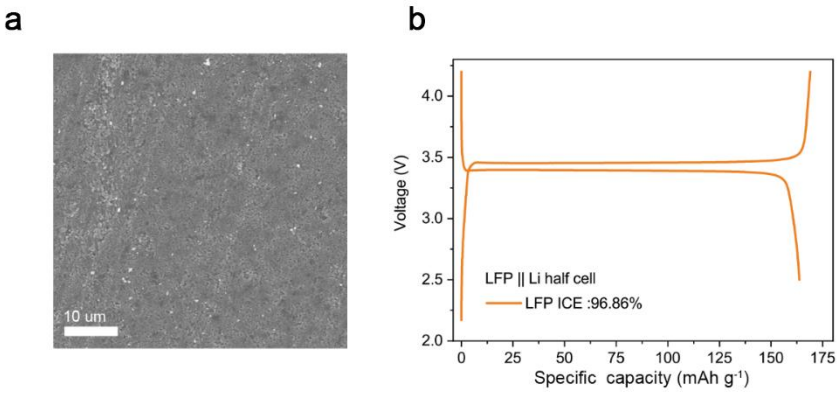


**Supplementary Figure 22** | **a**. Typical SEM image of the LFP electrode. **b**. Voltage profiles of the LFP half cell.

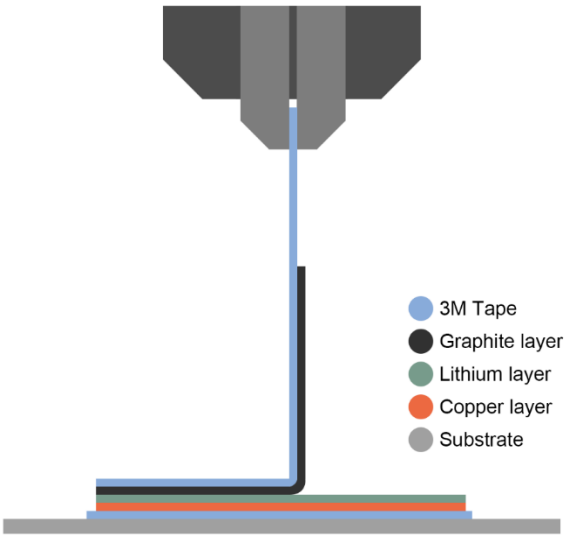


**Supplementary Figure 23** | Schematic illustration of peeling experiment. Details are seen in the Method.

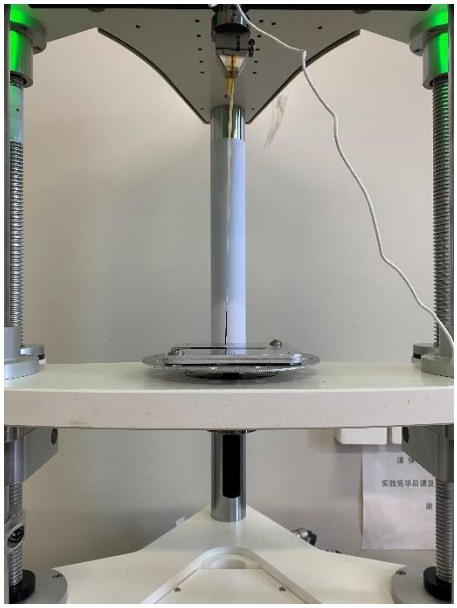

**Supplementary Figure 24** | A universal testing machine for peeling experiments. The graphite/stainless steel sample was loaded on the machine. See also the method.

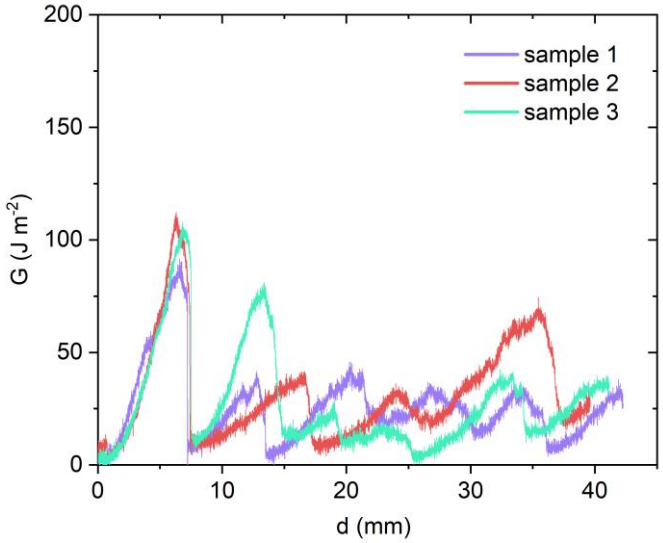


**Supplementary Figure 25 |** Energy release rate vs. peeling distance of interface between graphite and stainless-steel.

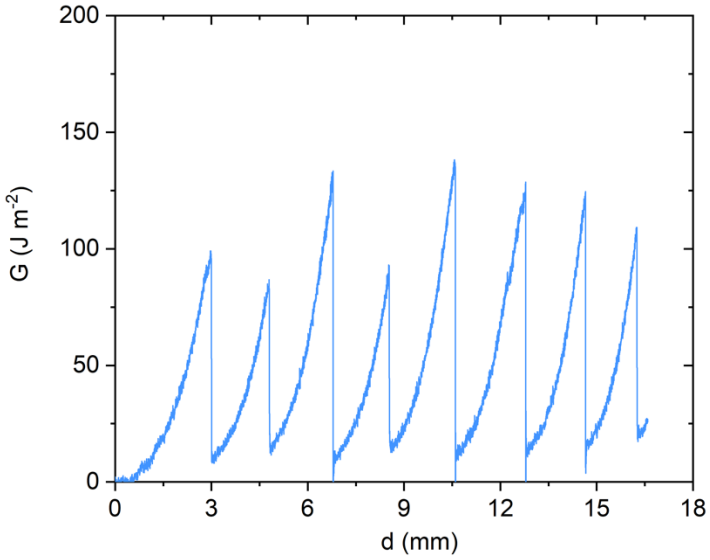


**Supplementary Figure 26** | Energy release rate vs. peeling distance of interface between graphite and lithium.

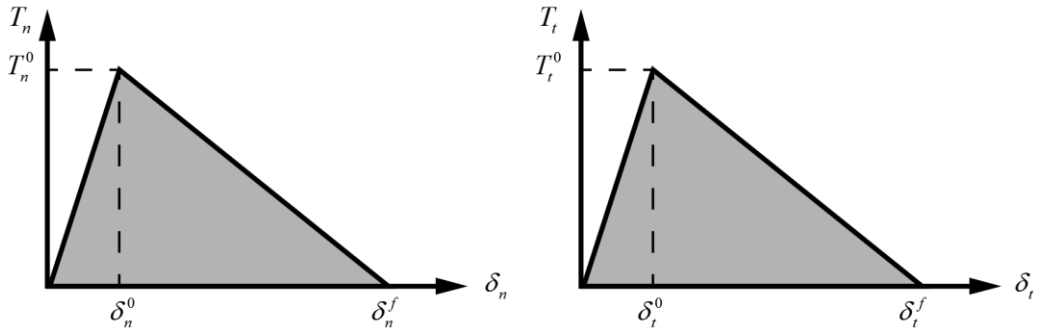


**Supplementary Figure 27** | Schematic illustrations of traction-separation laws of cohesive zones for mode I (opening) and II (shearing) interface fracture.

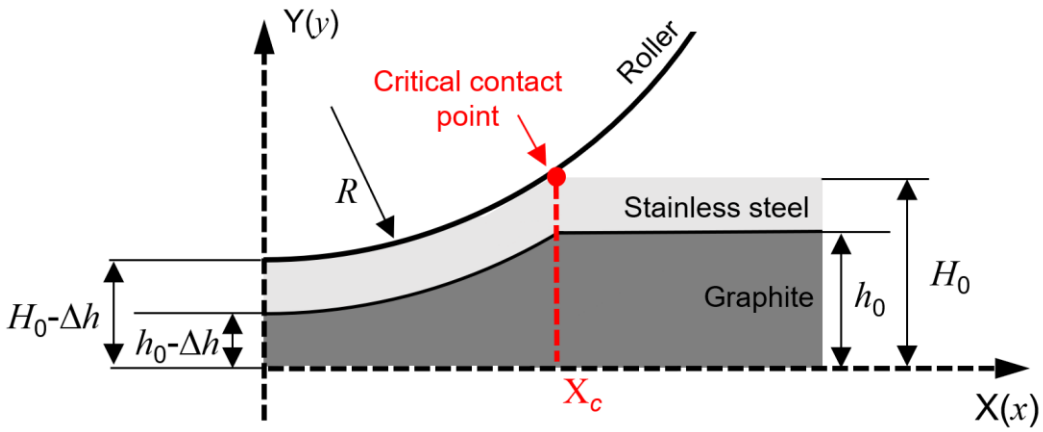


**Supplementary Figure 28 |** Schematic illustration of compression of electrode sample under a roller with a radius of *R*.

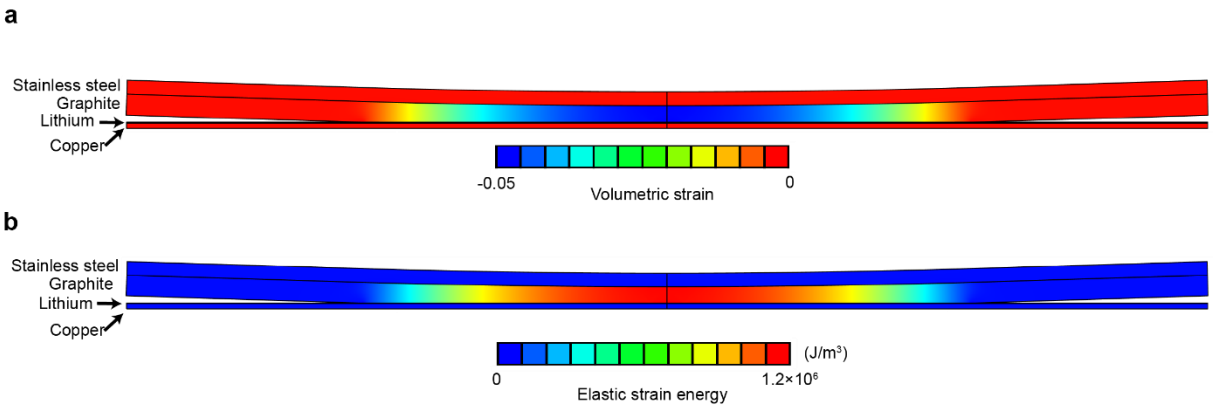


**Supplementary Figure 29 |** Distributions of volume strain and elastic strain energy of simulated sample from FE simulations.

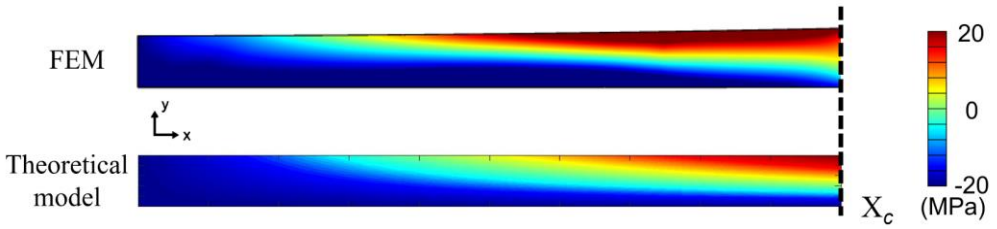


**Supplementary Figure 30 |** Comparison in shear stress distribution of graphite electrode from FE simulation and prediction based on a theoretical model. $X_c$ represents the critical contact point between the roller and compressed film.

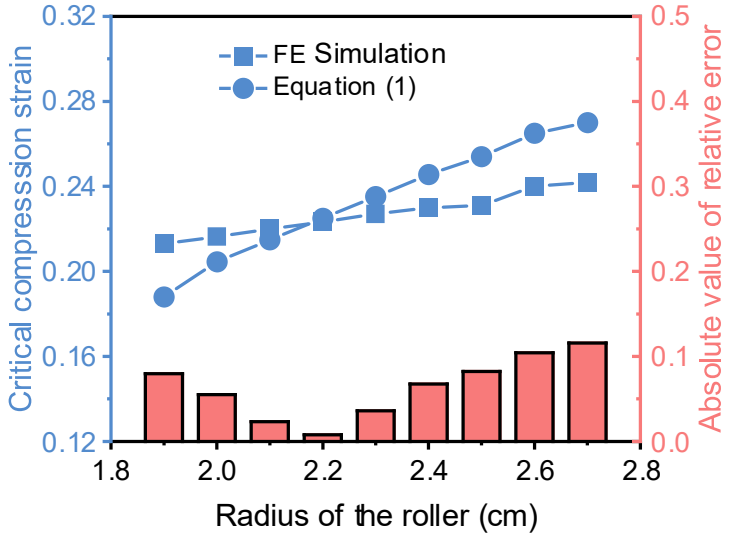


**Supplementary Figure 31** | Critical compressive strains from FE simulations and theoretical model and absolute values of their relative error as functions of radius of the roller.

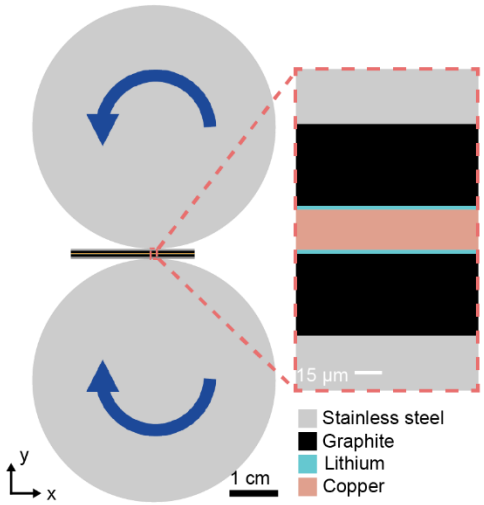


**Supplementary Figure 32 |** FE model for transfer-printing on the double-sided coated electrode.

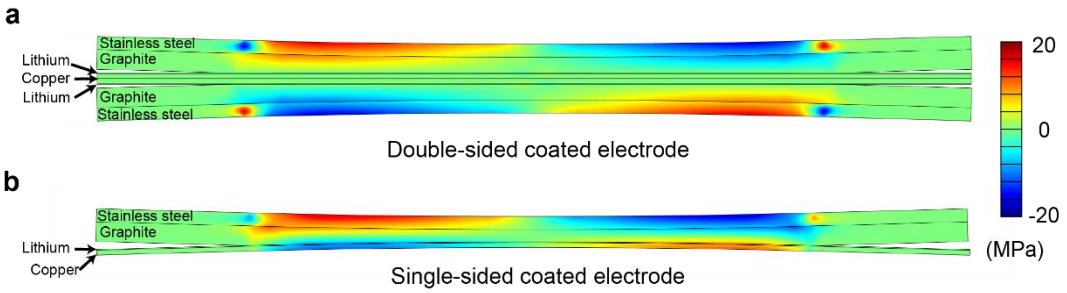


**Supplementary Figure 33 |** Comparison in shear stress distributions from FE simulations for double-sided and single-sided coated electrode samples. **a** Shear stress distribution in the double-sided coated electrode sample. **b**, Shear stress distribution in the single-sided coated electrode sample.

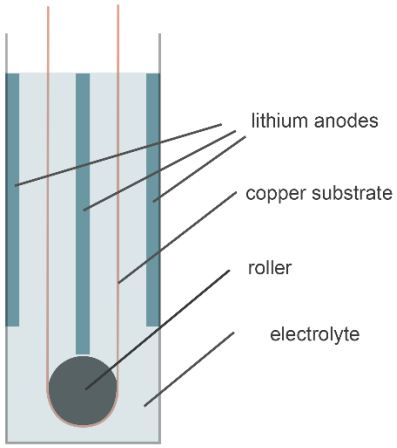


**Supplementary Figure 34 | The arrangement of electrodes in RET system.** The three lithium anodes were spaced 25 mm apart from one next to the other. The lithium anodes on both sides were 90 mm (vertical direction)×110 mm×2 mm (thickness). The lithium anodes in the middle were 100 mm (vertical direction)×110 mm (width)×2 mm (thickness). These anodes were covered with a celgard 2325 separator to avoid an unexpected short circuit. The roller was a cylinder of 25 mm in diameter. The width of the copper substrate is 100 mm.

**Supplementary Table 1. Parameters used in the FE modeling**

| Parameter | Symbol | Value | Unit |
|---|---|---|---|
| Elastic modulus of stainless steel | $E_{steel}$ | 194 | GPa |
| Elastic modulus of lithium | $E_{lithium}$ | 2 | GPa |
| Elastic modulus of copper foil | $E_{copper}$ | 119 | GPa |
| Poisson's ratio of stainless steel | $\nu_{steel}$ | 0.3 | |
| Poisson's ratio of lithium | $\nu_{lithium}$ | 0.36 | |
| Poisson's ratio of copper foil | $\nu_{copper}$ | 0.326 | |
| Shear modulus of graphite | $\mu_{graphite}$ | 300 | MPa |
| First Lamé constant of graphite | $\lambda_{graphite}$ | 300 | MPa |
| Yield strength of graphite | $\sigma^0_{graphite}$ | 40 | MPa |
| Critical energy release rate of the interface between stainless steel and graphite | $G^C_{n,steel-graphite}$ | 20 | J/m$^2$ |
| | $G^C_{t,steel-graphite}$ | 8 | J/m$^2$ |
| Critical energy release rate of the interface between graphite and lithium | $G^C_{n,graphite-lithium}$ | 100 | J/m$^2$ |
| | $G^C_{t,graphite-lithium}$ | 40 | J/m$^2$ |
| | $T^0_{n,steel-graphite}$ | 40 | MPa |

| | | | |
|---|---|---|---|
| Maximum traction of the interface between stainless steel and graphite | $T^0_{t,steel-graphite}$ | 16 | MPa |
| Maximum traction of the interface between graphite and lithium | $T^0_{n,graphite-lithium}$ | 200 | MPa |
| | $T^0_{t,graphite-lithium}$ | 80 | MPa |
| Friction coefficient between the roller and stainless steel | $f_{roller-steel}$ | 0.2 | |
| Friction coefficient between roller and copper foil | $f_{roller-copper}$ | 0.2 | |

**Supplementary Table 2. Cost and price estimations of RET system**

<table>
<tr><td></td><td colspan="3">Cost ($)</td></tr>
<tr><td></td><td colspan="2">Fabrication of prelithiation material (lithium)</td><td>Following rolling step</td><td>Assembling</td></tr>
<tr><td rowspan="2">Prelithiation by adding thin lithium foil</td><td>Commercialized 20-μm-thick Li metal foils price</td><td>12,327 $kg^{-1}$<br><br>Li foil need to be conducted by multiple micrometer-scale calendaring processes in an argon atmosphere, accounting for the vast majority of the cost.[1,2,3]</td><td rowspan="4">The thin lithium foil requires an additional rolling step to compress the lithium foil onto the anode materials, which share a similar cost with the transfer-printing step of our RET system.</td><td rowspan="4">The assembling cost is similar in these methods.</td></tr>
<tr><td>Total</td><td>12,327 $kg^{-1}$</td></tr>
<tr><td rowspan="2">Prelithiation by RET system</td><td>Large Li metal Ingot price</td><td>140~300 $kg^{-1}$<br><br>Commercialized product.[1,2,3]</td></tr>
<tr><td>Electrodeposition process and effluent treatment</td><td>20 $kg^{-1}$<br><br>Roll-to-roll electrodeposition and treatment of waste solution from electroplating are common in industrial production. The cost of electrochemical refining of copper is low than 0.1 \$ $kg^{-2}$.[4] The major cost of electrochemical deposition is the cost of consumption of electrolytes during electrodeposition. The prices of copper plating electrolytes and prices of lithium deposition electrolytes are 700 and 8000 \$ $t^{-1,}$ respectively.[5] The relative cost of</td></tr>
</table>

| | | | | |
|---|---|---|---|---|
| | | electrodeposition is insignificant compared with the cost of raw materials and Atmosphere. Considering these, we suppose the cost of the electrodeposition process and effluent treatment is no more than 20 \$ $kg^{-1}$. | | |
| | Argon atmosphere | 170 $kg^{-1}$<br><br>The manufacturing cost to maintain argon atmosphere (similar to 100-μm-thick Li metal foils). [1,2,3] | | |
| | Total | **330~490 $kg^{-1}$** | | |
| Prelithiation by adding SLMP | Commercialized SLMP price [3] | 16000 $kg^{-1}$ | The prelithiation by SLMP also needs an additional dispersion step and an additional rolling step to activate the reaction. These processes are more complex than the rolling process of our RET system. | |
| | Argon atmosphere | 170 $kg^{-1}$<br><br>The manufacturing cost to maintain argon atmosphere (similar to 100-μm-thick Li metal foils). [1] | | |
| | Total | 16170 $kg^{-1}$ | | |
| Chemical prelithiation | Prelithiation reagent cost | 264~424 $kg^{-1}$ The price of the prelithiation reagent cost was given by the chemical products | The Chemical prelithiation needs to | |

| | | | | |
|---|---|---|---|---|
| with Li/Naph/DME | | trading platform.[5] The recipe of prelithiation reagent was given as 10 mmol lithium and 10 mmol Naph in 10 ml DME.[6] | follow electrode infiltration steps and electrode cleaning steps. These processes are complex than the rolling process of our RET system. | |
| | Preparation of prelithiation reagent | 1 $kg^{-1}$ | | |
| | Argon atmosphere | 170 $kg^{-1}$<br><br>The manufacturing cost to maintain argon atmosphere (similar to 100-μm-thick Li metal foils) [1,2,3] | | |
| | Total | **436~596 $kg^{-1}$** | | |
| Electrochemical prelithiation | The cost of electrochemical prelithiation is hard to estimate due to its difficulty in implementation and its complexity of process. | | | |

**Supplementary References**


1. Chen, H. et al. Free-standing ultrathin lithium metal–graphene oxide host foils with controllable thickness for lithium batteries. Nature Energy **6**, 790–798 (2021).

2. Li product. Shang Hai Ou Jin Industrial Co. Ltd.

   http://www.sh-oujin.com/ProductShow.asp?ID=557

3. Ultrathin Li foil and S LMP products. *Cellithium*

   http://www.cellithium.com/blank01.html

4. Staff, Han Lu, *Platts Metal Daily* **11**, 127-9-9 (2022).

5. Chemical products. https://www.alibaba.com/

6. Shen, Y., Qian, J., Yang, H., Zhong, F. & Ai, X. Chemically prelithiated hard-carbon anode for high power and high capacity Li-ion batteries. *Small* **16**, (2020).